Atomistic structure and three-dimensional spatial distribution of oxide clusters along voids in nitride metal/semiconductor superlattices

Rajendra Kumar [1], Limei Yang,[2] Ingrid McCarroll,[2] S. M. Shivaprasad,[1,4] Julie M. Cairney,[2,3]
Magnus Garbrecht [2], and Bivas Saha [1,4,*]

[1]*Chemistry and Physics of Materials Unit and International Centre for Materials Science, Jawaharlal Nehru Centre for Advanced Scientific Research, Jakkur, Bangalore-560064, India*
[2]*Australian Centre for Microscopy and Microanalysis, The University of Sydney, New South Wales 2006, Australia*
[3]*School of Aerospace, Mechanical and Mechatronic Engineering, The University of Sydney, Camperdown, New South Wales 2006, Australia*
[4]*School of Advanced Materials, Jawaharlal Nehru Centre for Advanced Scientific Research, Jakkur, Bangalore-560064, India*

Epitaxial metal/semiconductor superlattices with atomically sharp interfaces and tunable Schottky barrier heights have attracted significant interest in recent years for thermionic emission-based high-temperature thermoelectric devices, optical hyperbolic metamaterials, hot-electron photocatalysis, and optoelectronic heterostructures for visible-to-terahertz frequency range applications. ZrN/ScN is a demonstration of such epitaxial metal/semiconductor superlattices and exhibits atomically sharp lattice-matched interfaces, albeit with the presence of threading dislocations on MgO substrates. Along with its influence on structural integrity and atomic diffusion, the presence of such defects significantly impacts electron and phonon transport in these metamaterials with carrier trapping, scattering, shunt path, etc. Therefore, an in-depth analysis of the atomistic structure and the composition of such defects is extremely necessary to design devices with improved efficiencies. In this paper, high-resolution scanning transmission electron microscopy and atom-probe tomography are employed to determine the structure and three-dimensional (3D) spatial distribution of oxide defect clusters along the voids in ZrN/ScN superlattices. ScO^+ and ScO^{++} ions are found to cluster predominantly along such 3D interface defects with zirconium and scandium atoms surrounding them. Defect regions are also found to be depleted of nitrogen atoms and rich with a high concentration of oxygen. The oxygen content was found to be higher inside the ScN layers compared to ZrN. First-principles modeling analysis verified the clustering of oxygen at high oxygen partial pressure and demonstrated a higher affinity of scandium towards oxygen than for zirconium towards oxygen. These results mark significant progress in understanding the atomic structure and composition of defects in nitride superlattices.

I. INTRODUCTION

Epitaxial metal/semiconductor superlattice heterostructures with tunable Schottky barrier heights have enormous potential for applications in highly efficient thermionic emission-based thermoelectric devices [1–3], terahertz optoelectronics, optical hyperbolic metamaterials [4,5], hot-electron based solar-energy converters [6,7] and photodetectors [8]. However, the development of low-defect density single-crystalline metal/semiconductor superlattices has been challenging due to the requirement of lattice-matched metallic and semiconducting materials with the same crystal structures, similar homologous temperature, and low excess surface and interface energy densities [9]. Epitaxial ZrN/ScN metal/semiconductor superlattices with sharp interfaces have been developed [4,10] that exhibit a Schottky barrier height of ~0.28 eV, and a large Seebeck coefficient of 820 μV/K at room temperature, as required for thermionic emission devices [3,11,12]. In addition, cross-plane thermal conductivity measurement showed that the superlattices exhibit about

2.7 times lower thermal conductivity in comparison to the mean lattice thermal conductivities of the constituent materials due to enhanced incoherent phonon scattering at the interfaces which is essential for thermoelectric applications [13]. Theoretical calculations incorporating the experimental results predict a high thermoelectric figure of merit (*ZT*) of 1.5 at 1300 K in ZrN/ScN superlattices when the electron lateral momentum is conserved and a *ZT* of more than 3 is achievable if the momentum is not conserved [12]. Efforts are also underway to control the electronic transport with doping and alloying, and with quantum size effects [14,15]. While ZrN/ScN superlattice thin films exhibit promising transport properties for waste heat to electrical energy conversion [11], the control of extended defects and reducing the defect densities remain a challenge. Reproducible transport measurements also require the superlattices to be free from extended defects. Due to ~7% lattice mismatch with MgO substrates, ZrN/ScN superlattices exhibit a high density $(10^{11} \mathrm{cm}^{-2})$ of threading dislocations along the growth directions [16]. Subsequent thermal annealing was found to trigger dislocation pipe diffusion along the threading dislocations that eventually lead to metallic shunt path formation for electron conduction [10].

*bsaha@jncasr.ac.in

Void formation along planar defects in thin films during the growth or in the course of device operation is detrimental for their performance [17–19] and may result in device failures [20]. During the growth, voids can emerge at column boundaries in thin films due to reduced adatom mobility at low growth temperatures and shadowing effects [3,21]. Voids can also form during high-temperature device operation due to both interdiffusion of metal atoms across the interface with different diffusion constants, known as the Kirkendall effect [22], and diffusion of vacancies in the films, or in the course of the amorphization process in phase-change memory devices, caused by mass transport in the presence of an electric field [23]. Although the presence of voids can be helpful in reducing the dislocation densities by acting as dislocation sinks, thus improving the crystalline quality of the overgrown films [24], cross-plane transport will be reduced since electron and phonon propagation are impacted by carrier trapping and scattering. For example, formation of voids at the interface between AlN/sapphire during thermal annealing result in polarity inversion of AlN, which limits potential device performance [17,18]. The presence of voids in $Cu(In, Ga)Se_2$ solar cells leads to degradation of their performance [19]. The formation of voids during the cycling process in $Ge_2Sb_2Te_5$-based phase-change random access memory results in the cell failure [20]. Kirkendall void formation within intermetallic layers of solder joints can be critical for their reliability in chip-scale electronic packaging as the failure of solder joints will result in the failure of the whole microelectronic system [25–27].

The void regions in individual transition metal nitride semiconductors such as ScN have been found to accommodate a high concentration of unwanted impurities such as oxygen [3,28], which results in its high *n*-type carrier concentration (10^{20}–10^{21} cm^{-3}), resulting in a narrow depletion width (2–3 nm) at the ZrN/ScN interfaces. Such a narrow depletion width results in tunneling electrical contact and prevents the observation of thermionic emission. Thus, it is extremely important to understand the nature and composition of voids in ZrN/ScN superlattices and determine their impact on the structural and electronic properties.

Here we introduced voids in ZrN/ScN superlattices by reducing the growth temperature, thereby reducing the adatom mobility and enhancing the Ehrlich-Schwoebel barrier, thus promoting the columnar growth. Clustering of oxygen defects around the voids of ZrN/ScN metal/semiconductor superlattices is directly observed with high-resolution scanning transmission electron microscopy (HRSTEM), energy-dispersive x-ray spectroscopy (EDS), and atom-probe tomography (APT) techniques. First-principles density functional theory (DFT) simulations are utilized to model the energetic tendency of oxygen to cluster in ScN and ZrN in the presence of defects. Modeling also predicts the site preference of oxygen defects in these materials, which matches well with experimental observations.

II. METHODS

A. Material growth

An epitaxial ZrN/ScN metal/semiconductor superlattice with a period thickness of 20 nm was deposited on a MgO (001) substrate using a dc-magnetron sputtering system (PVD Products, Inc.) in a bottom-up confocal arrangement with a base pressure of 4×10^{-8} Torr. A 1 μm ZrN buffer layer was deposited on a (001) MgO substrate before the multilayer growth. Prior to film deposition, the MgO substrate was degreased with acetone and methanol. The substrate temperature was maintained at 750 °C throughout the deposition to achieve a high density of voids. High-purity metal targets of Sc (99.998%) and Zr (99.99%) having dimensions of 2 in. diameter and 0.25 in. thickness were used. An Ar/N_2 mixture of 6 SCCM Ar and 4 SCCM (SCCM denotes "cubic centimeter per minute at STP") N_2 at a deposition pressure of 5 mTorr was maintained during the deposition.

B. Sample preparation

TEM lamellae and APT needles were prepared with a ThermoFisher Helios Xe Plasma focused ion beam/scanning electron microscope (FIB/SEM) and Zeiss Auriga Ga ion FIB/SEM. Samples were coated with a 25 nm Au coating to prevent charging. A 500 nm Pt protective cap was deposited for both TEM and APT lift-outs. TEM lamellae were prepared on the Helios using a 30 kV accelerating voltage with a 60 nA current, followed by 15 nA for trenching and lift-out. The TEM lift-out specimens were welded to Mo grids. Thinning was achieved with tilt angles of $\pm 2°$ and a beam current of 1 nA. Final thinning was at $\pm 2°$ and 300 pA, checking for electron transparency using a 2 kV electron beam with a Secondary Electron (SE) detector. When the region of interest (ROI) was thin enough a 5 kV polish at 30 pA and $\pm 3°$ was used to remove beam induced damage. The TEM lamellae were prepared and thinned yielding both MgO [010] and [110] orientations. Samples were prepared for APT using the backside lift-out preparation method [29]. Initial milling of the wedge for lift-out was conducted on the Helios using a 30 kV accelerating voltage and either 16 or 15 nA current. After initial 2 μm $\times$ 2 μm blanks were deposited on a W grid, the samples were transferred to the Zeiss Auriga for final annular milling. The final APT tips with apex diameters <100 nm were prepared using an accelerating voltage of 10 kV and a current of 50 pA.

C. Scanning transmission electron microscopy

The STEM images and EDS maps were recorded employing an image- and probe-corrected and monochromated Themis-Z 60–300 kV instrument equipped with a high-brightness X-FEG (field emission gun) source and Super-X EDS detector system for ultrahigh count rates, operated at 300 kV. The Super-X EDX detector system enables the recording of high spatial resolution EDS maps. The EDS maps contain arrays of individual spectra as large as a $4k \times 4k$ pixel, and color codes the elemental peak of the highest intensity for each spectrum/pixel as shown in the map. EDS maps with total counts well above 5 000 000 have been recorded for quantification. Absorption correction and applying the *k*-factor method yields a precision of about 1–2 at. % content in an area of known sample thickness at that count rate, provided no peak overlaps are present.

D. Atom-probe tomography

Atom-probe tomography data were acquired on a laser assisted CAMECA local electrode atom probe (LEAP) 4000X Si. Two datasets are presented herein, the parameters used for the first dataset, Fig. 3(a), were 100 pJ laser energy, a 200 kHz pulse frequency, an ion detection rate of 0.5%, and a temperature of 60 K. The parameters for the second dataset, Fig. 3(b), were 50 pJ laser energy, 100 kHz pulse frequency, an ion detection rate of 1.0%, and a stage temperature of 60 K. The parameters were changed as part of a parameter sweep to determine ideal run conditions for analysis of the ZrN/ScN superlattice. Reconstruction of APT data was completed using IVAS 3.8.6. As a result of the changing evaporation field requirements for the ScN and ZrN layers, it was necessary to reconstruct the tip using the "shank" reconstruction algorithm; this algorithm assumes a constant shank angle along the length of the atom-probe tip.

E. Computational details

The formation energies of various oxygen and native defects and their complexes were calculated with total energy calculations using *ab initio* density functional theory (DFT) as implemented in the SIESTA code [30]. Norm-conserving pseudopotentials of Troullier and Martins [31] were used with the valence electron configurations of scandium, zirconium, nitrogen, and oxygen as $3d^1 4s^2$, $4d^2 5s^2$, $2s^2 2p^3$, and $2s^2 2p^4$, respectively. The exchange and correlation energy functional was approximated using the generalized gradient approximation (GGA) method proposed by Perdew *et al.* [32]. A basis set of atomic orbitals is constructed using a double zeta function with polarization. The Hartree and exchange-correlation energies were estimated using a uniform grid of points in real space with a maximum kinetic energy of 200 Ry. The Brillouin zone of the conventional eight-atom unit cell in reciprocal space of ZrN and ScN was sampled using Γ-centered k-point meshes of $12 \times 12 \times 12$ and $15 \times 15 \times 15$, respectively. For structure optimization all the atoms were allowed to relax until the forces on each atom were less than 0.02 eV/Å. For oxygen defects in ScN and ZrN, a $3 \times 3 \times 3$ supercell with 216 atoms was constructed. The formation energy of various oxygen-related defects was calculated using the Zhang-Northrup scheme [33], which is given by

$$E_F(\text{def}) = E_{\text{tot}}(\text{def}) - E_{\text{tot}}(\text{pristine}) + \sum_i x_i \mu_i, \quad (1)$$

where $E_{\text{tot}}(\text{pristine})$ is the total energy of a pristine supercell; $E_{\text{tot}}(\text{def})$ is the total energy of a supercell, including the defect. x_i is the number of atoms added (or removed) in the pristine supercell to form the defect supercell. μ_i is the chemical potential of the element added to or removed from the pristine supercell to form a defect supercell. The chemical potential of nitrogen (μ_N) at nitrogen-rich conditions was obtained using Eq. (2) while the chemical potential of oxygen (μ_O) was calculated at both oxygen-rich and oxygen-poor conditions using Eqs. (3a), (3b), and (3c), respectively.

$$\mu_N = E_{\text{tot}}(N) - D_0(N). \quad (2)$$

In oxygen-rich conditions,

$$\mu_O = E_{\text{tot}}(O) - D_0(O). \quad (3a)$$

In oxygen-poor conditions,

$$\mu_O = E_{\text{tot}}(\text{Zr}_3\text{O}) - 3 \times \mu_{\text{Zr}} \quad \text{for ZrN,} \quad (3b)$$

and

$$\mu_O = \tfrac{1}{3}[E_{\text{tot}}(\text{Sc}_2\text{O}_3) - 2 \times \mu_{\text{Sc}}] \quad \text{for ScN,} \quad (3c)$$

where $E_{\text{tot}}(N)$ and $E_{\text{tot}}(O)$ are atomic energies of N and O atoms, calculated by placing a single atom in a large supercell with a vacuum of more than 25 Å in all three directions, and breaking the cubic symmetry by having different lattice constants in different directions. $D_0(N)$ and $D_0(O)$ represent the experimental dissociation energy of nitrogen (9.80 eV) [34] and oxygen (5.16 eV) [34], respectively. $E_{\text{tot}}(\text{Zr}_3\text{O})$ is the total energy of Zr_3O in the hexagonal crystal system. $E_{\text{tot}}(\text{Sc}_2\text{O}_3)$ is total energy of Sc_2O_3 in a cubic crystal system. μ_{Zr} and μ_{Sc} are chemical potentials of Zr and Sc, respectively, calculated in their respective metallic form. The maximum defect concentration in a $3 \times 3 \times 3$ supercell with 216 atoms is $\sim$2.3% which is less than the experimental oxygen concentrations.

The binding energy of various defect complexes ($n\text{O}_N$ and $n\text{O}_N + \text{O}_i$) is calculated using the following equation:

$$E_b(n\text{O}_N + \text{O}_i) = nE_F(\text{O}_N) + E_F(\text{O}_i) - E_F(n\text{O}_N + \text{O}_i). \quad (4)$$

Further, a 2×2 in-plane supercell with eight layers each of ScN and ZrN having 256 atoms was considered to calculate the formation energy $E_F(\text{def})$ of oxygen defects in the ZrN/ScN superlattices. For the comparison of formation energy of oxygen defects in the ZrN/ScN superlattice, the formation energy of oxygen defects in bulk ScN and ZrN was also calculated using a $2 \times 2 \times 2$ supercell with 64 atoms.

III. RESULTS AND DISCUSSION

A. HRSTEM EDS analysis

The high-angle annular dark-field (HAADF) STEM image of the ZrN/ScN superlattices deposited on MgO/ZrN buffer layer (Fig. 1) shows a sharp and coherent ZrN buffer/MgO interface; however, parallel dark lines spaced $\sim$30–40 nm apart appear above 200–300 nm from the MgO substrate. These lines run straight through the buffer layer and terminate at the buffer/superlattice interface, resulting in the formation of columns in the buffer. A higher-magnification STEM micrograph in Fig. 1(b) shows that the dark contrast lines are voids decorating the side facets of the columns and have a width of between 5 and 20 nm. HRSTEM images of these void regions are presented in Fig. S1 of the Supplemental Material (SM) [35]. A detailed study on the structure and composition of these voids was performed in our previous article on the TiN/Al$_{0.72}$Sc$_{0.28}$N superlattice [21]. While most of those voids terminate at the buffer/superlattice interface, a few of them extend into the superlattice as in Fig. 1(b). The presence of the voids is a result of the relatively low growth temperature (750 °C) compared to the previously used 850 °C [10], which leads to lower adatom mobility and a
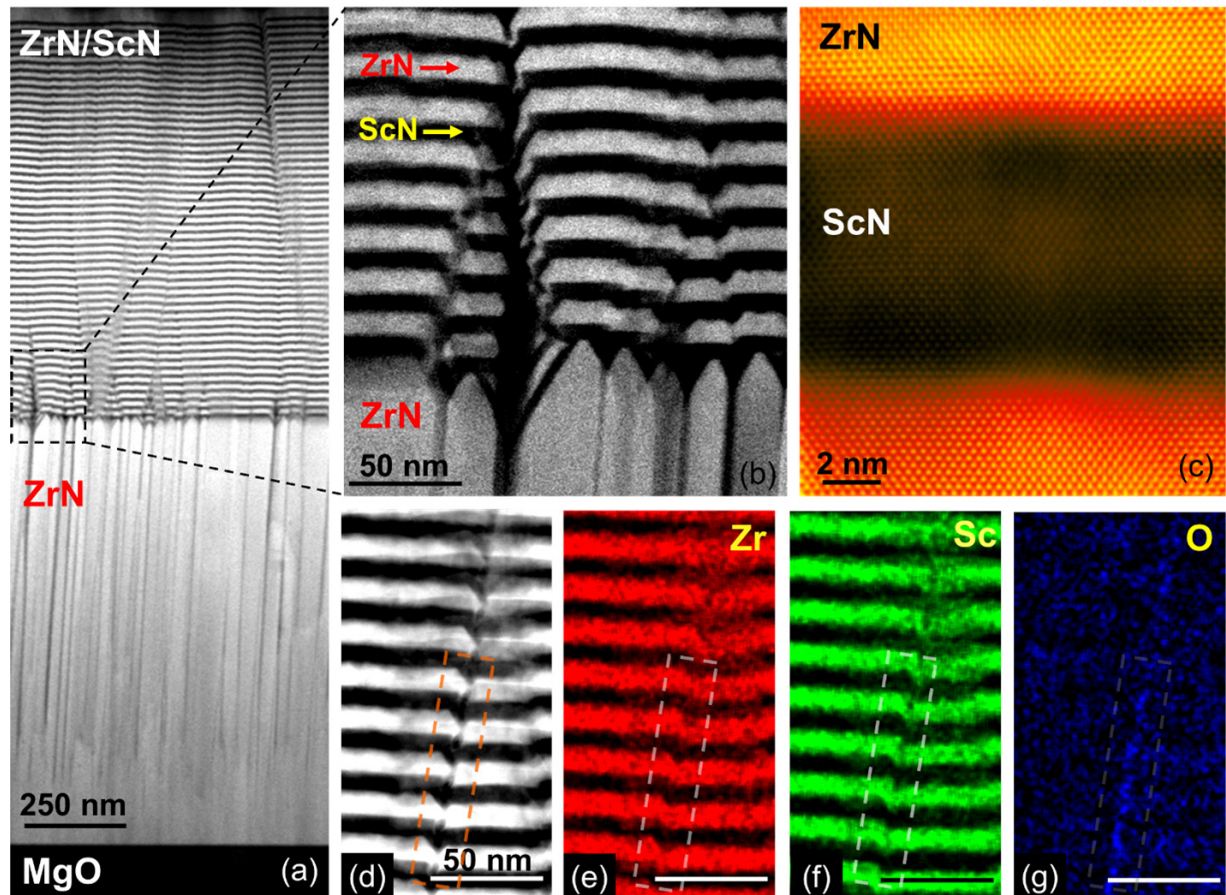
FIG. 1. (a) HAADF STEM image of the ZrN/ScN superlattice with ZrN buffer layer on MgO (001) substrate. Panel (b) shows the ZrN buffer layer's columnar growth and resulting pyramid-shaped surface. While most column boundaries decorated by voids terminate at the buffer/superlattice interface, a few extend into the superlattice. (c) Color scale atomic-resolution STEM image of ZrN/ScN recorded along the [110] direction demonstrating flat interfaces. (d) HAADF STEM and EDS maps of Zr (e), Sc (f), and O (g), showing clustering of oxygen along the voids.

relatively high Ehrlich-Schwoebel barrier [28]. Away from the voids, the layers are found to maintain their epitaxial relationship and display nearly sharp interfaces with Sc and Zr intermixing of less than two unit cells as demonstrated by the atomic-resolution STEM micrograph Fig. 1(c) recorded along the [110] direction higher up in the superlattice stack. A STEM image [Fig. 1(d)] and corresponding Sc (Fig. 1(e)], Zr [Fig. 1(f)], and O [Fig. 1(g)] EDS elemental maps from a region of a column boundary decorated by voids show a kink in the layers, attributed to a slightly different pace of growth in the adjacent column. Voids are located along the centerline of that kink, and oxygen atoms are found to cluster there over a width of about 5 nm [Fig. 1(g)].

The oxygen content inside the intact layers away from the voids was determined quantitatively by extracting integrated line profiles from the EDS maps [see Figs. 2(a) and 2(b)]. Background correction to the hyperspectral map data is applied using an empirical model employing Brown-Powell ionization cross section, *k*-factor method, and absorption correction to the entire spectral cube, and a Gaussian filter with sigma 1.0 is applied as a postfilter for smoothing of the map images. The line profiles are further smoothed with fast Fourier transform (FFT) filtering to remove the high-frequency noise in the data. The results reveal a nonuniform

distribution of oxygen inside the superlattice [see Fig. 2(c)]. ZrN layers contain an average oxygen concentration of $\sim$6–7 at. %, but ScN layers exhibit oxygen concentration of $\sim$8–8.5 at. %. Zr and Sc atomic concentrations are found to oscillate as expected though the exact Sc concentration cannot be accurately determined due to the overlap of Sc and N peaks in EDS. The O edge does not overlap with any neighboring elements (see Fig. S2 in the SM [35]). Using *k*-factor methods and absorption correction, the oxygen concentration obtained using EDS is reliable with an error bar of $\sim$1.35%.

B. APT analysis

To further investigate the nature of oxygen clustering around the void region, APT is conducted on a sharp needle prepared from the ZrN/ScN superlattice [see Fig. 3(a)] in a region that contains voids similar to that shown in Fig. 1(d). During an atom-probe run, time of flight data and the *x* and *y* ion positions are collected. The tomographic reconstruction process is based on the Bas *et al.* [36] back projection algorithm and the *z* coordinates are based on the order of atom detection. The time of flight data are converted into a mass to charge state ratio. Combined, this data produces a chemically-resolved three-dimensional ion-by-ion reconstruction of the
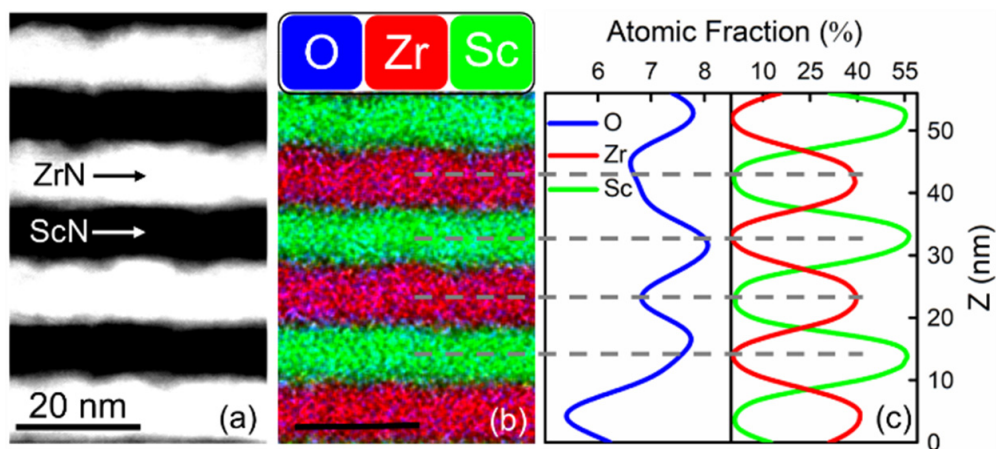
FIG. 2. (a) HAADF STEM of the superlattice, (b) corresponding combined O, Sc, and Zr EDS map. (c) Atomic concentration profiles of Sc, Zr, and O after integration of spectra along full width of the layers given in (b). The raw data without FFT smoothing of the concentration profile is presented in Fig. S3 of the SM [35],indicating that the oxygen concentration profile has an error bar of ∼1.35%.

initial tip Fig. 3(a). The reconstructed three-dimensional (3D) atom map provides further insight into the oxygen distribution within the ZrN and ScN layers of the superlattice. Figure 3(a) shows the presence of a high concentration of oxygen evaporated from the atom-probe tip in the form of ScO within

the voids. The yellow surfaces displayed in Fig. 3(a) are iso-concentration surfaces of 6 at. % combined ScO$^+$ and ScO^{++} peaks. The concentration of oxygen is higher inside these surfaces and lower outside. Full three-dimensional visualization of the features is available in the videos in the SM [35]. From
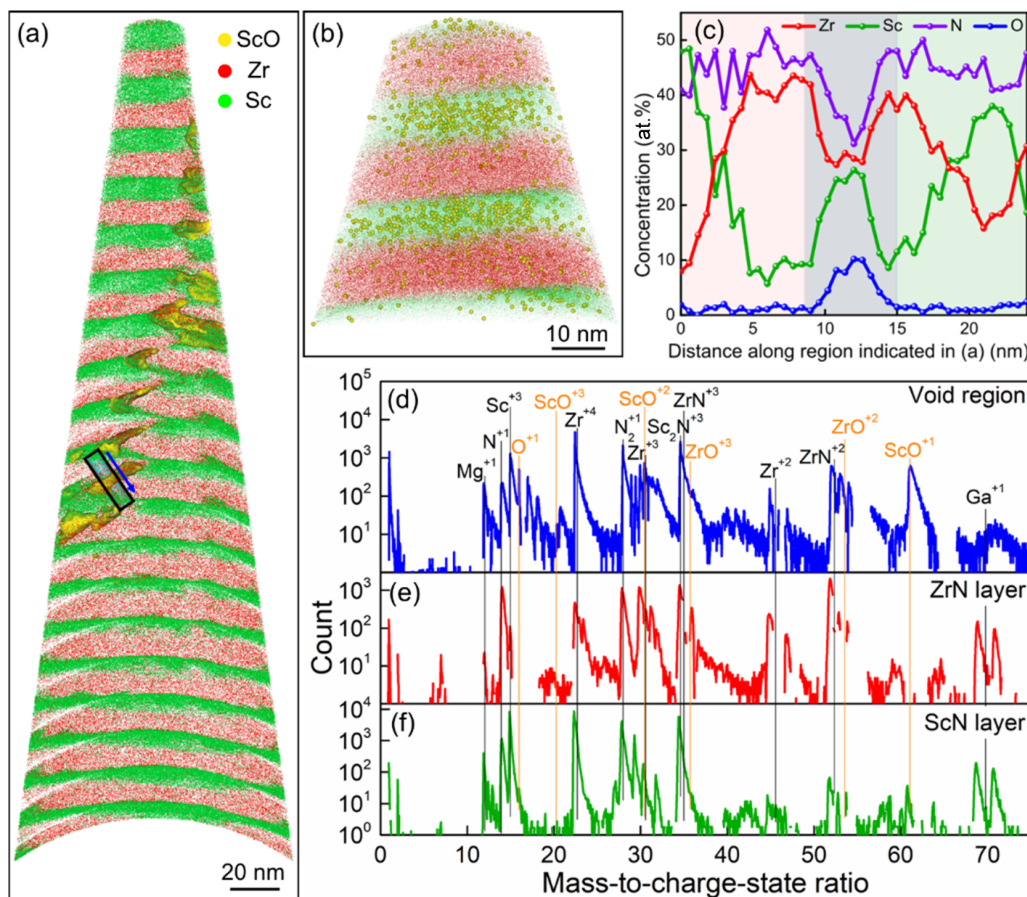

FIG. 3. Panel (a) shows 6 at. % isoconcentration surface of ScO in a 10 nm section of the data. (b) High-resolution APT mapping of a tip exhibiting formation of ScO in ScN layers. (c) One-dimensional concentration profile along the region marked in (a). Mass spectrum corresponding to the (d) void region, (e) ZrN layer, and (f) ScN layer.

Fig. 3(a) it can also be seen that the regions containing the ScO ions contain both zirconium and scandium. Away from the void, ScO^+ and ScO^{++} ions are found with larger concentrations inside the ScN layers [as shown in Fig. 3(b)] than in the ZrN layers. For more clarity on relative concentration of O in ScN and ZrN layers, the ScO ions in Fig. 3(b) are shown separately from the Zr and Sc ions in Fig. S4 of the SM [35]. While oxygen looks to be present inside the ZrN layers, it is most likely the result of noise at the location of the ScO^+ and ScO^{++} peaks. Zr-O or O ions were not observed in the ZrN layer. Therefore, the APT data indicate a higher concentration of oxygen within the ScN layer, consistent with the STEM EDS mapping.

A one-dimensional concentration profile through the voids, as shown in Figs. 3(a) and 3(c), reveals that the defect is enriched with approximately 10–11 at. % of oxygen. Therefore, the oxygen concentration is almost double inside the voids compared to the ZrN layers and about 50% higher than in ScN. The concentration profile also supports the observation of both zirconium and scandium at the voids and a decrease in the nitrogen content. The depletion of nitrogen provides additional experimental evidence of the substitution of oxygen for nitrogen within the voids in ZrN/ScN nitride superlattices. In regions near the voids, the ZrN and ScN layers contain very low oxygen and do not show significant variations between the layers, confirming local diffusion of oxygen to the voids. Note that Fig. 3(c) refers to a region that is close to a defect (void) and therefore it does not represent the oxygen concentration within the defect-free regions of the ZrN or ScN layers. Similar clustering of oxygen near defect-containing voids has been previously observed in ScN films deposited with molecular beam epitaxy [28]. Recently it has been reported that O forms clusters in the form of ScO_x or ScO_xN_y in ScN films [37], and postgrowth exposure of ScN in air results in oxide formation at the surface [38]. The oxygen concentration in bulk ScN due to postgrowth exposure to air strongly depends on crystalline defects and grain boundaries in the films [28,38], as it is easier for oxygen to diffuse along defect lines and grain boundaries. Cunha *et al.* [39] have also shown the presence of Zr-N-O phases in ZrN_xO_y films deposited using radio-frequency reactive magnetron sputtering.

A breakdown of the mass spectrum is performed at various locations in the ZrN/ScN superlattice, and the O peaks are distinguished in Figs. 3(d)–3(f). The mass spectrum from the void region shows clear peaks corresponding to ScO ions [see Fig. 3(d)]. Also, the intensity of the mass to charge ratio corresponding to ScO ions is higher around the void region compared to the ScN and ZrN layers in the superlattice, suggesting the formation of ScO clusters around the void region.

C. DFT formation energy

To understand the origin of the higher concentration of oxygen in ScN than in ZrN and the clustering of oxygen in the form of ScO, we have performed *first-principles* DFT simulations. Modeling analysis revealed lattice parameters of 4.61 and 4.52 Å, respectively, for ZrN and ScN, which is close to the experimentally observed value of 4.59 Å for ZrN and 4.51 Å for ScN.

The substitutional oxygen defect (O_N), where one nitrogen atom was replaced with one oxygen atom in a $3 \times 3 \times 3$ supercell with 216 atoms (see Figs. S5(a) and S5(e) in the SM [35]) exhibited formation energies of -2.78 and -4.64 eV in oxygen-rich conditions for ZrN and ScN, respectively. An interstitial oxygen (O_i) defect was most stable at the tetrahedral site in ZrN [$E_F(O_i) = -0.65$ eV], and at the split interstitial site along the [111] direction in ScN [$E_F(O_i) = 0.66$ eV] among all possible interstitial configurations (see Figs. S5(b) and S5(f) in the SM [35]). Further, various defect complexes of oxygen such as nO_N and $nO_N + O_i$ in both ScN and ZrN were considered. The formation energy of these defect complexes decreased with increasing n and exhibited a value of -14.33 and -19.08 eV for the $4O_N + O_i$ defect complex in oxygen-rich conditions in ZrN and ScN, respectively. In ScN, the position of O_i in the $nO_N + O_i$ defect complex is very sensitive to n and shifts towards the tetrahedral site with increasing n from its initial split interstitial site in $O_N + O_i$.

The dependence of the oxygen-defect formation energy on the chemical potential of oxygen (or O_2 partial pressure) was calculated and is presented in Fig. 4. At a very low oxygen partial pressure (below 10^{-12} Torr), O_N is the most stable defect in ZrN, albeit with positive formation energy [see Fig. 4(c)]. Similarly, below 10^{-20} Torr oxygen partial pressure, O_N is the most stable defect in ScN. Under experimental growth conditions ($\sim 10^{-9}$ Torr), $4O_N + O_i$ is the most stable oxygen-defect complex in ZrN, whereas $4O_N$ appears to be the most stable in ScN. In extreme O-rich conditions, $4O_N + O_i$ is the most stable defect in both ZrN and ScN. Also, for the entire partial pressure range, oxygen defects exhibit lower formation energy in ScN than in ZrN, indicating a stronger affinity of O towards ScN compared to ZrN, which results in higher O incorporation in ScN layers compared to ZrN layers during growth as observed in the STEM EDS mapping and APT. Along with background oxygen in the growth chamber, oxygen can also be incorporated in the films by target contaminations, impurities in process gases, and limited atom mobility during growth, causing pyramidal growth with exposed facets at which oxygen can accumulate [28,40,41]. Thus, the experimental oxygen concentration in the deposited films could be slightly larger than the expected concentration at background oxygen partial pressure in 10^{-9} Torr, and accordingly the $4O_N + O_i$ defect complex could be the most stable defect in ScN. At nominal O concentrations, oxygen will cluster in both ZrN and ScN to form Zr-N-O and Sc-N-O phases, and when the oxygen concentration crosses a threshold in some region, it will form separate ZrO_2 or Sc_2O_3 phases [42]. The ZrN/ScN superlattice sample does not show any separate phase corresponding to ZrO_2 or Sc_2O_3 in the XRD pattern [3]. However, there appears to be an increased presence of O in the form of ScO in the defect regions, demonstrating the formation of oxide clusters [see Figs. 1(g) and 3(a)]. Similar clustering of oxygen point defects has also been reported in other transitional metal nitrides [43].

D. Defect-complex binding energy

To further clarify the formation of defect complexes, the binding energies of nO_N and $nO_N + O_i$ in both ScN and ZrN are presented in Table I, which is calculated using Eq. (4). The
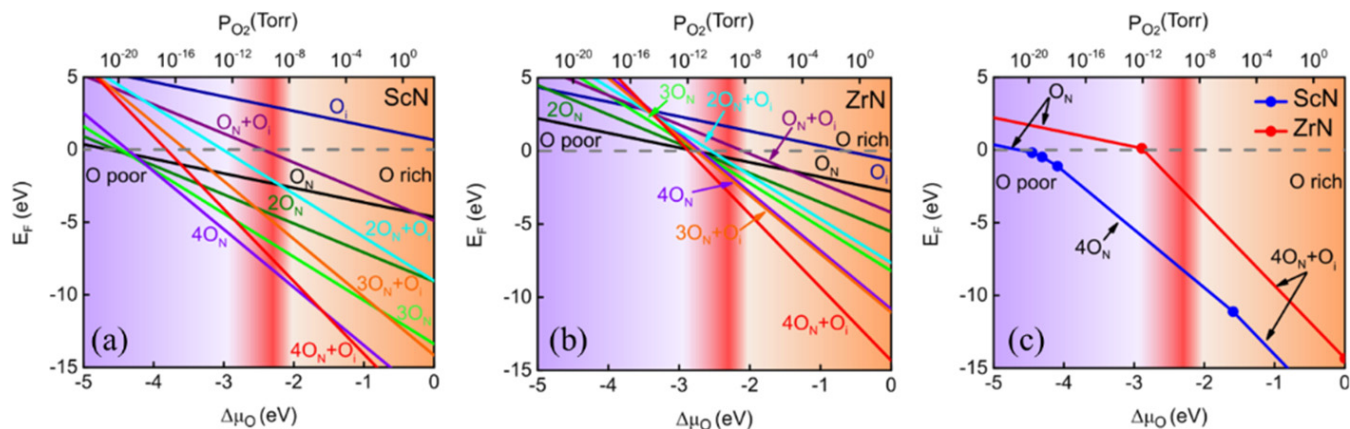
FIG. 4. The formation energy of various oxygen defects as a function of the chemical potential of oxygen (partial pressure of O_2) in ScN (a), ZrN (b). Panel (c) shows the most stable O defect configuration at a given partial pressure in ScN and ZrN. The red shaded region corresponds to background oxygen partial pressure in the sputtering chamber.

binding energy of nO_N defect complexes is negative in both ScN and ZrN, which suggests that these defect complexes are not strongly bound and will prefer to either disintegrate in isolated O_N defects or transform into defect complexes having positive binding energy. However, $nO_N + O_i$ defect complexes exhibit positive binding energy in both ScN and ZrN. Thus, such defect complexes will be more favorable to stabilize inside the materials.

E. Influence of interfaces on O_N formation energies

In order to verify the effect of superlattice interfaces, the formation energy of oxygen defects in various layers of ZrN/ScN superlattices was calculated. Results show that the formation energy of an O_N defect is minimum at the fourth layer (furthest from the interface) of ScN in an eight-layer/eight-layer ZrN/ScN superlattice (see Table II). However, the formation energy was found to be 0.23 eV higher than calculated for the bulk ScN, which could be a result of O's interaction with the interface region. Further, as the oxygen defect was inserted within the ZrN layers of the superlattice, the defect formation energy of O_N increased and exhibited a maximum at the fourth layer of ZrN from the interface. Thus, the calculation supports that oxygen defects will be more stable in ScN than ZrN inside the ZrN/ScN superlattice, and ScN is expected to contain more oxygen

than ZrN inside the superlattice, which agrees well with our experimental results.

IV. CONCLUSIONS

In conclusion, STEM EDS and APT are used to directly visualize oxide defect clusters along engineered voids in lattice-matched ZrN/ScN metal/semiconductor superlattices. Clusters of ScO^+ and ScO^{++} are found to occupy the void regions with Sc and Zr atoms surrounding these regions. The ScN layer exhibited a higher concentration of ScO^+ and ScO^{++} than ZrN. First-principles density functional theory simulations support the experimentally observed clustering of oxygen defects and also shows a higher affinity of ScN towards oxygen compared to ZrN. These results mark significant progress in understanding the role of oxygen contamination and its distribution within nitride metal/semiconductor superlattice heterostructures and will help inform the design of devices with improved functionality.

TABLE I. Binding energy of various nO_N and $nO_N + O_i$ defect complexes. High positive energy corresponds to a strongly bound complex.

Configuration	Binding energy (eV)	
	ScN	ZrN
$2O_N$	−0.20	−0.05
$3O_N$	−0.54	−0.15
$4O_N$	−1.09	−0.32
$O_N + O_i$	0.91	0.76
$2O_N + O_i$	0.42	1.43
$3O_N + O_i$	0.90	2.02
$4O_N + O_i$	1.18	2.54

TABLE II. Formation energy of O_N defect in the ZrN/ScN superlattice

O_N defect position with respect to interface in ZrN/ScN superlattice	Defect formation energy (eV)
First layer of ScN	−3.26
Fourth layer of ScN	−4.27
First layer of ZrN	−3.02
Fourth layer of ZrN	−2.82

[1] Z. Bian and A. Shakouri, Appl. Phys. Lett. **88**, 012102 (2006).

[2] D. Vashaee and A. Shakouri, Phys. Rev. Lett. **92**, 106103 (2004).

[3] M. Garbrecht, I. McCarroll, L. Yang, V. Bhatia, B. Biswas, D. Rao, J. M. Cairney, and B. Saha, J. Mater. Sci. **55**, 1592 (2020).

[4] B. Saha, G. V. Naik, S. Saber, C. Akatay, E. A. Stach, V. M. Shalaev, A. Boltasseva, and T. D. Sands, Phys. Rev. B **90**, 125420 (2014).

[5] G. V. Naik, B. Saha, J. Liu, S. M. Saber, E. A. Stach, J. M. K. Irudayaraj, T. D. Sands, V. M. Shalaev, and A. Boltasseva, Proc. Natl. Acad. Sci. U. S. A. **111**, 7546 (2014).

[6] E. Rephaeli and S. Fan, Opt. Express **17**, 15145 (2009).

[7] M. Sakhdari, M. Hajizadegan, M. Farhat, and P. Y. Chen, Nano Energy **26**, 371 (2016).

[8] H. Srour, J. P. Salvestrini, A. Ahaitouf, S. Gautier, T. Moudakir, B. Assouar, M. Abarkan, S. Hamady, and A. Ougazzaden, Appl. Phys. Lett. **99**, 221101 (2011).

[9] B. Saha, A. Shakouri, and T. D. Sands, Appl. Phys. Rev. **5**, 021101 (2018).

[10] M. Garbrecht, J. L. Schroeder, L. Hultman, J. Birch, B. Saha, and T. D. Sands, J. Mater. Sci. **51**, 8250 (2016).

[11] B. Saha, T. D. Sands, and U. V. Waghmare, J. Appl. Phys. **109**, 083717 (2011).

[12] M. Zebarjadi, Z. Bian, R. Singh, A. Shakouri, R. Wortman, V. Rawat, and T. Sands, J. Electron. Mater. **38**, 960 (2009).

[13] V. Rawat, Y. K. Koh, D. G. Cahill, and T. D. Sands, J. Appl. Phys. **105**, 024909 (2009).

[14] S. Nayak, M. Baral, M. Gupta, J. Singh, M. Garbrecht, T. Ganguli, S. M. Shivaprasad, and B. Saha, Phys. Rev. B **99**, 161117(R) (2019).

[15] B. Saha, J. A. Perez-Taborda, J. H. Bahk, Y. R. Koh, A. Shakouri, M. Martin-Gonzalez, and T. D. Sands, Phys. Rev. B **97**, 085301 (2018).

[16] M. Garbrecht, B. Saha, J. L. Schroeder, L. Hultman, and T. D. Sands, Sci. Rep. **7**, 46092 (2017).

[17] N. Stolyarchuk, T. Markurt, A. Courville, K. March, O. Tottereau, P. Vennéguès, and M. Albrecht, J. Appl. Phys. **122**, 155303 (2017).

[18] L. Hussey, R. M. White, R. Kirste, S. Mita, I. Bryan, W. Guo, K. Osterman, B. Haidet, Z. Bryan, M. Bobea, R. Collazo, and Z. Sitar, Appl. Phys. Lett. **104**, 032104 (2014).

[19] E. Avancini, D. Keller, R. Carron, Y. Arroyo-Rojas Dasilva, R. Erni, A. Priebe, S. Di Napoli, M. Carrisi, G. Sozzi, R. Menozzi, F. Fu, S. Buecheler, and A. N. Tiwari, Sci. Technol. Adv. Mater. **19**, 871 (2018).

[20] C.-F. Chen, A. Schrott, M. H. Lee, S. Raoux, Y. H. Shih, M. Breitwisch, F. H. Baumann, E. K. Lai, T. M. Shaw, P. Flaitz, R. Cheek, E. A. Joseph, S. H. Chen, B. Rajendran, H. L. Lung, and C. Lam, in *Proceedings 2009 IEEE International Memory Workshop* (IEEE, New York, 2009), pp. 1–2.

[21] M. Garbrecht, L. Hultman, M. H. Fawey, T. D. Sands, and B. Saha, Phys. Rev. Mater. **1**, 033402 (2017).

[22] A. D. Smigelskas and E. O. Kirkendall, Trans. AIME **171**, 130 (1947).

[23] T. Y. Yang, J. Y. Cho, Y. J. Park, and Y. C. Joo, Acta Mater. **60**, 2021 (2012).

[24] P. Frajtag, N. A. El-Masry, N. Nepal, and S. M. Bedair, Appl. Phys. Lett. **98**, 023115 (2011).

[25] D. Kim, J. H. Chang, J. Park, and J. J. Pak, J. Mater. Sci. Mater. Electron. **22**, 703 (2011).

[26] K. Weinberg, T. Böhme, and W. H. Müller, Comput. Mater. Sci. **45**, 827 (2009).

[27] Z. Mei, M. Ahmad, M. Hu, and G. Ramakrishna, in *Proceedings Electronic Components and Technology, 2005 (ECTC '05)* (IEEE, New York, 2005), Vol. 2, pp. 415–420.

[28] D. Rao, B. Biswas, S. Acharya, V. Bhatia, A. I. K. Pillai, M. Garbrecht, and B. Saha, Appl. Phys. Lett. **117**, 212101 (2020).

[29] T. J. Prosa, D. Lawrence, D. Olson, D. J. Larson, and E. A. Marquis, Microsc. Microanal. **15**, 298 (2009).

[30] J. M. Soler, E. Artacho, J. D. Gale, A. García, J. Junquera, P. Ordejón, and D. Sánchez-Portal, J. Phys.: Condens. Matter **14**, 2745 (2002).

[31] N. Troullier and J. L. Martins, Phys. Rev. B **43**, 1993 (1991).

[32] J. P. Perdew, K. Burke, and M. Ernzerhof, Phys. Rev. Lett. **77**, 3865 (1996).

[33] S. B. Zhang and J. E. Northrup, Phys. Rev. Lett. **67**, 2339 (1991).

[34] K. P. Huber and G. Herzberg, Molecular Spectra and Molecular Structure (Springer US, Boston, 1979).

[35] See Supplemental Material at http://link.aps.org/supplemental/10.1103/PhysRevMaterials.5.084601 for HRSTEM image of void, EDS spectrum of the superlattice, atomic representation of defects, and three-dimensional representation of oxygen clustering near void regions.

[36] P. Bas, A. Bostel, B. Deconihout, and D. Blavette, Appl. Surf. Sci. **87–88**, 298 (1995).

[37] A. L. le Febvrier, N. Tureson, N. Stilkerich, G. Greczynski, and P. Eklund, J. Phys. D: Appl. Phys. **52**, 035302 (2019).

[38] J. More-Chevalier, S. Cichoň, L. Horák, J. Bulíř, P. Hubík, Z. Gedeonová, L. Fekete, M. Poupon, and J. Lančok, Appl. Surf. Sci. **515**, 145968 (2020).

[39] L. Cunha, F. Vaz, C. Moura, L. Rebouta, P. Carvalho, E. Alves, A. Cavaleiro, P. Goudeau, and J. P. Rivière, Surf. Coat. Technol. **200**, 2917 (2006).

[40] D. Rao, B. Biswas, E. Flores, A. Chatterjee, M. Garbrecht, Y. R. Koh, V. Bhatia, A. I. K. Pillai, P. E. Hopkins, M. Martin-Gonzalez, and B. Saha, Appl. Phys. Lett. **116**, 152103 (2020).

[41] C. Höglund, J. Bareño, J. Birch, B. Alling, Z. Czigány, and L. Hultman, J. Appl. Phys. **105**, 113517 (2009).

[42] Z. B. Qi, Z. T. Wu, H. F. Liang, D. F. Zhang, J. H. Wang, and Z. C. Wang, Scr. Mater. **97**, 9 (2015).

[43] R. Kumar, S. Nayak, M. Garbrecht, V. Bhatia, A. Indiradevi Kamalasanan Pillai, M. Gupta, S. M. Shivaprasad, and B. Saha, J. Appl. Phys. **129**, 055305 (2021).